Biomass wood-derived efficient Fe–N–C catalysts for oxygen reduction reaction

Dingding Li, Zheng Han, Kunyue Leng, Shenghua Ma, Yi Wang, Jinbo Bai

▶ To cite this version:

Dingding Li, Zheng Han, Kunyue Leng, Shenghua Ma, Yi Wang, et al.. Biomass wood-derived efficient Fe–N–C catalysts for oxygen reduction reaction. Journal of Materials Science, 2021, 56 (22), pp.12764-12774. ⟨10.1007/s10853-021-06122-7⟩. ⟨hal-03390217⟩

HAL Id: hal-03390217

https://hal.science/hal-03390217v1

Submitted on 4 Nov 2021

Biomass Wood-Derived Efficient Fe-N-C Catalysts for Oxygen Reduction Reaction

Dingding Li,[a] Zheng Han,[a] Kunyue Leng,[a] Shenghua Ma,[a] Yi Wang,*[a] and Jinbo Bai*[b]

[a] *State Key Laboratory of Photoelectric Technology and Functional Materials, International Collaborative Center on Photoelectric Technology and Nano Functional Materials, Institute of Photonics & Photon-Technology, Northwest University, Xi'an, 710069, PR China.*

[b] *Université Paris-Saclay, CentraleSupélec, CNRS UMR8579, Laboratoire de Mécanique des Sols, Structures et Matériaux, 91190, Gif-sur-Yvette, France.*

*Corresponding author

E-mail address: yi.wang@nwu.edu.cn jinbo.bai@centralesupelec.fr

Abstract

Efficient and low cost electrocatalysts for oxygen reduction reaction (ORR) was the key for scalable application of metal-air batteries and fuel cells. Herein, iron-based nitrogen doped carbon catalysts (Fe-N-C_{wood}) was prepared, using hydrothermal-pyrolysis treated wood-derived nitrogen doped carbon as the support. This support possessed large specific surface area and macro-meso-micro hierarchical porous networks, ensuring fluent mass transfer of electrolyte and oxygen species. In the ORR electrochemical test, Fe-N-C_{wood} catalyst showed an excellent activity, with a half-wave potential of 0.90 V in 0.1 M KOH, and a half-wave potential of 0.70 V in 0.1 M $HClO_4$. Moreover, durability tests illustrated that Fe-N-C_{wood} possessed high stability and methanol tolerance. The Fe-N-C_{wood} based Zn-air battery delivered a peak power density of 231 mW cm^{-2}, suggesting its potential applications in sustainable energy conversion systems.

Introduction

Fuel cells and metal-air batteries were considered as one of the most promising sustainable energy conversion systems that required highly efficient catalysts for oxygen reduction reaction (ORR) at the cathode.[1-5] Hitherto, platinum-based materials were the most widely used cathode catalysts for ORR.[6] Unfortunately, the scarcity, high cost and poor methanol tolerance of platinum severely hindered its widespread commercial applications.[7-10] To overcome the challenge, increasing attention had been attracted to search high-performance platinum-free ORR catalysts. Among the multifarious candidates, transition metal-based nitrogen doped porous carbon (M-N-C) materials were regarded as one promising alternative.[11-14]

In general, the porous structure of M-N-C catalysts significantly influenced its mass transfer ability, which was another key determined the ORR activity, in addition to the active sites. [7,15,16] Many studies have been made on this topic, which demonstrated that the ORR activity of M-N-C were significantly influenced by the specific surface area, [17-19] as well as the ratio of micropore, mesopore, and even macropore in catalyst.[20,21] These current achievements inspired the efforts of tuning the porous structure of M-N-C to gain desired ORR performance. However, it was still a challenge to design and construct efficient mass transfer hierarchical structure, because the rational hierarchical structure was also related to pore morphology, pore branching and precise diameter ratios for connecting multi-scale pores from macro to micro levels.[15,22]

Recently, biomass-derived carbon materials have been extensively explored in electrocatalysts and supercapacitors, mainly due to the renewable and sustainable property. [23-26] In the view of hierarchical structure, biomass exhibited rational hierarchical structure designed and optimized by the nature, ensuring fluent mass transfer throughout the network. [22] Nevertheless, the nature hierarchical structure of biomass would be partially destroyed during pyrolysis and metal impregnation. The advanced ORR catalysts usually derived from special biomass resources such as pollen [27] and peanut hull [28], which reduced its application potentials. As one of the most abundant biomass resources, wood was held great potential to overcome this challenge. [25,29,30] However, the ORR catalysts based on wood-derived carbons were generally moderate in performance. Herein, we adopt a hydrothermal-pyrolysis method to prepare N-doped carbon support, using the trunk of koelreuteria paniculate as the carbon source. In the electrochemical tests, the obtained catalyst exhibited excellent activity, with a half-wave potential of 0.90 V in 0.1 M KOH, and a half-wave potential of 0.70 V in 0.1 M $HClO_4$.

Results and discussion

Figure 1 showed the morphology of wood derived carbon material (Fe-N-

C_{wood}). Scanning electron microscopy (SEM) images revealed that Fe-N-C_{wood} exhibited similar morphology compared with the wood-derived carbon support (N-C_{wood}, Figure 1a-b). Transmission electron microscopy (TEM, Figure 1c) and the corresponding electron energy loss spectroscopy (EELS, Figure 1d) revealed that iron nanoparticles were homogeneously dispersed over Fe-N-C_{wood}. The lattice distance of iron nanoparticles in Fe-N-C_{wood} was measured at 0.204 nm, corresponding to Fe_3C (220) planes or Fe (110) planes.[31] Figure 1e and Figure 1f showed the morphology information of Fe-N-C_{XC-72} prepared by the same method using the commercial carbon support XC-72 (Figure S3).

Figure 2 showed the X-ray diffraction (XRD) patterns of XC-72, Fe-N-C_{XC-72}, N-C_{wood} and Fe-N-C_{wood}. The peak at 26.1° in XC-72, Fe-N-C_{XC-72}, N-C_{wood} and Fe-N-C_{wood} could be attributed to graphitic carbon (002) plane, and the peaks situated at 43.7° and 44.7° in Fe-N-C_{XC-72} and Fe-N-C_{wood} were corresponding to Fe_3C (102) plane (35-0772) and Fe (110) plane (06-0696). The high-resolution Fe 2p, N 1s and C 1s X-ray photoelectron spectroscopy of Fe-N-C_{wood} were shown in Figure 2b, Figure 2c and Figure 2d, respectively. In the Fe 2p XPS spectrum (Figure 2b), the signals of 707.1 and 720.1 eV could be assigned to Fe $2p_{3/2}$ and Fe $2p_{1/2}$ from zero-valent Fe.[32] The signals at 710.5 and 722.7 eV could be assigned to Fe $2p_{3/2}$ and Fe $2p_{1/2}$ from Fe(II) species.[33] The signals at 714.2 and 726.4 eV could be assigned to Fe $2p_{3/2}$ and Fe $2p_{1/2}$ from Fe(III) species.[33] In the N 1s XPS spectrum (Figure 2c), four peaks were observed at 398.3, 399.8, 401.0 and 402.5 eV, which could be attributed to pyridinic nitrogen, pyrrolic nitrogen, graphitic nitrogen and oxide nitrogen, respectively.[3,26] In the C 1s XPS spectrum (Figure 2d), three peaks of 284.6, 285.3 and 288.6 eV were observed, which could be attributed to the C-C, C-N and C=O groups, respectively (Figure 2d).[3] The survey scan XPS spectra as well as the C 1s and N 1s XPS spectrum for N-C_{wood} were shown in Figure S4-S7, respectively. The proportion of Fe was similar for Fe-N-C_{wood} and Fe-N-C_{XC-72}, in line with ICP-OES results (Table S1). Figure 2f and Figure 2e showed the N_2 isotherms of XC-72, Fe-N-C_{XC-72}, N-C_{wood} and Fe-N-C_{wood}, and the detailed data were presented in Table S1. N-C_{wood} showed the specific surface area of 2004.8 m^2/g (S_{micro} = 301.9 m^2/g and S_{extern} = 1702.9 m^2/g, Table S1), which was decreased to 840.9 m^2/g (S_{micro} = 378.4 m^2/g and S_{extern} = 462.5 m^2/g) for Fe-N-C_{wood}. This decreased surface area in Fe-N-C_{wood} was attributed to the loss of external surface area, suggesting that iron was mainly deposited on the external surface. Further, the pore size distributions and mercury intrusion porosimetry indicated that Fe-N-C_{wood} possessed mesopores centered at about 4 nm (Figure S8) and macropores centered at about 1.3 µm (Figure S9). In comparison, the specific surface area of XC-72 and Fe-N-C_{XC-72} were 240.5 m^2/g and 131.5 m^2/g, respectively.

The catalytic evaluation of Fe-N-C_{wood} was firstly tested in 0.1 M KOH at

O_2 saturated condition. The cyclic voltammetry (CV) curve (Figure S10) showed that, Fe-N-C_{wood} exhibits obvious characteristics peak at 0.84 V in the O_2 saturated condition, which was not found in the N_2 saturated condition. Linear scanning of the voltammogram (LSV) curve in the O_2-saturated condition (Figure 3a) showed that Fe-N-C_{wood} had excellent ORR activity, its half-wave potential ($E_{1/2}$) reached 0.90 V and the onset potential (E_{onset}) was 0.98 V. In comparison, the half-wave potentials for Pt/C, Fe-N-C_{XC-72}, XC-72 and N-C_{wood} were 0.83, 0.80, 0.67 and 0.78 V (Figure S11), respectively, and the onset potentials for Pt/C, Fe-N-C_{XC-72}, XC-72 and N-C_{wood} were 0.96, 0.90, 0.78 and 0.88 V, respectively. The kinetic current density (j_k) of Fe-N-C_{wood} at 0.9 V was calculated at 2.43 mA cm^{-2} (Figure S12), which was significantly higher than Pt/C (0.81 mA cm^{-2}) and Fe-N-C_{XC-72} (0.27 mA cm^{-2}). Moreover, the Tafel slope of Fe-N-C_{wood} was calculated at 80 mV dec^{-1}, which was significantly lower than that of Pt/C (90 mV dec^{-1}) and Fe-N-C_{XC-72} (102 mV dec^{-1}) (Figure 3b and Figure S13), suggesting again the higher activity of the wood-derived catalyst. Importantly, the activity of Fe-N-C_{wood} in alkaline media outperformed most of biomass-derived catalysts, as shown in Table 1.

Figure 3c showed the LSV curve measured at different rotation rates, and the corresponding Koutecky-Levich (KL) diagram was shown in Figure S14. The yields of peroxide (%) for Fe-N-C_{wood} were monitored by RRDE measurements on the Pt ring (Figure 3d). As a result, the peroxide yield for

$Fe-N-C_{wood}$ was less than 3.8%, and the election transfer number was between 3.9 and 4.0. Moreover, the stability of $Fe-N-C_{wood}$ was tested by chronoamperometry and electrochemical accelerated durability test (EADT). In the EADT, the activity of $Fe-N-C_{wood}$ was not significantly decreased after 5,000 cycles (Figure 3e). On contrary, a significant negative shift was observed in Pt/C catalyst (Figure S15). In the chronoamperometry test (Figure 3f), $Fe-N-C_{wood}$ lost 2% of current after 10 000 s, while Pt/C lost around 30% of the original current. Furthermore, Figure S16 showed the methanol tolerance of $Fe-N-C_{wood}$ was measured by the chronoamperometric response with the presence of methanol. The current of Pt/C decreased during the addition of methanol, but the current of $Fe-N-C_{wood}$ was not lost. These results illustrated the high stability of wood-derived catalyst in ORR applications with alkaline media.

In Figure S17, $Fe-N-C_{wood}$ shows an oxygen reduction peak in 0.1 M $HClO_4$ at O_2 saturated condition, indicating that $Fe-N-C_{wood}$ possessed ORR activity in acidic electrolytes. At 1600 rpm, $Fe-N-C_{wood}$ exhibited a $E_{1/2}$ of 0.70 V and E_{onset} of 0.81 V, which was worse than Pt/C but much better than $Fe-N-C_{XC-72}$, XC-72 and $N-C_{wood}$ (Figure 4a and Figure S18). The Tafel slope as well as the LSV curves of wood-derived catalyst at different rotation rates were shown in Figure 4b and Figure 4c. Its electron transfer number in the acidic media was between 3.92 and 4 (Figure 4d). Table 2 compared the ORR activity of this catalyst with some other noble metal free catalysts. Moreover, Fe-N-C$_{wood}$ exhibited good stability in the EADT and chronoamperometry tests (Figure 4e, 4f and Figure S19).

Zn-air battery test was carried out using Fe-N-C$_{wood}$ coated carbon paper cathode and zinc foil anode. Zn-air battery with Fe-N-C$_{wood}$ catalyst exhibited a peak power density of 231 mW cm^{-2} (Figure 5a), which was higher than that with Pt/C catalyst (204 mW cm^{-2}) and most of other catalysts (Table 3). The specific discharge capacity of Zn-air battery with Fe-N-C$_{wood}$ catalyst at 50 mA cm^{-2} was 726.9 mAhg^{-1} (Figure 5b), larger than that with Pt/C catalyst (626.8 mAhg^{-1}). The Fe-N-C$_{wood}$ cathode in liquid zinc-air battery provided an open circuit potential of 1.434 V (Figure 5c). Two batteries in series can effectively make the LED lamp (8 mm, 3.2 V) work (Figure 5d). The good performance of Fe-N-C$_{wood}$ in Zn-air battery again confirmed the excellent activity of Fe-N-C$_{wood}$ in ORR.

As known, active site was the key that influenced the activity of catalysts,[7] and the iron phthalocyanine was a conventional iron precursor for high performance Fe-N-C catalyst.[34] It could be observed that the impregnation of Fe greatly decreased the external surface area of resultant catalyst. Through the optimization of N-C$_{wood}$ by adding Na_2CO_3 during pyrolyzing process, its external surface area was greatly increased (the function of Na_2CO_3 was shown in Figure S21), which compensated the loss of external surface after Fe impregnation. The combination of highly efficient actives sites and hierarchical structure resulted in the high activity of Fe-N-C_{wood}. The developed synthetic approach paved a low-cost, readily scalable route for the preparation of high-performance ORR catalyst.

Conclusions

In summary, a wood-derived carbon embedded with iron nanoparticles catalyst exhibited high catalytic reactivity in ORR reaction. The obtained Fe-N-C_{wood} catalyst showed a half wave potential of 0.90 V in 0.1M KOH and a half wave potential at 0.70 V in 0.1M $HClO_4$. Meanwhile, this catalyst possessed impressive stability and methanol tolerance. The resultant Zn-air battery with Fe-N-C_{wood} catalyst showed an outstanding peak power density of 231 mW cm^{-2}. The superior catalytic performances of Fe-N-C_{wood} could be attributed to the highly efficient Fe active sites and its rational hierarchical porous structure with micropores (S_{micro} = 378.4 m^2/g), mesopores (S_{extern} = 462.5 m^2/g, centered at about 4 nm) and macropores (centered at about 1.3 μm).

Experimental

N-C_{wood} was prepared by fresh wood powder (koelreuteria paniculate). CH_3COOH, H_2O_2 and H_2O were mixed for hydrothermal reaction, and the resulting product was pyrolyzed with Na_2CO_3 and urea under a high-purity Ar flow (800°C, 3 hours) to obtain N-C_{wood}.

Fe-N-C_{wood} was prepared by the following method. FePc and N-C_{wood} were added to acetone, stirred and evaporated to dryness, and then pyrolyzed under a high-purity Ar flow (900°C, 1 hours). The resulting sample was labeled as Fe-N-C_{wood}.

Fe-N-C_{XC-72} was obtained through the preparation process of Fe-N-C_{wood} by replacing N-C_{wood} with XC-72.

Details of preparation, characterizations and electrochemical tests were presented in the Supporting Information.

Conflicts of interest

The authors declare no competing financial interest.

Acknowledgements

This work was supported by the National Natural Science Foundation of China (51873134), Natural Science Foundation of Shaanxi Province (2018JQ5058), Industrial Innovation China of Key Research, Development Project of Shaanxi Province (2019ZDLGY16-09) and the Scientific Research Project of Education Department of Shaanxi Province (20JK0945).

Electronic Supplementary Material: The online version of this article (http://dx.doi.org/10.1007/s12274-***-****-*) contains supplementary material, which is available to authorized users.

Reference

[1] Li YJ, Cui L, Da PF et al (2018) Multiscale Structural Engineering of Ni-Doped CoO Nanosheets for Zinc–Air Batteries with High Power Density. Adv Mater 30 (46):1804653

[2] Mu C, Mao J, Guo J et al (2020) Rational design of spinel cobalt vanadate oxide Co_2VO_4 for superior electrocatalysis. Adv Mater 32 (10):1907168

[3] Ma S, Han Z, Leng K et al (2020) Ionic Exchange of Metal-Organic Frameworks for Constructing Unsaturated Copper Single-Atom Catalysts for Boosting Oxygen Reduction Reaction. Small:2001384

[4] Sun C, Alonso JA, Bian J (2021) Recent advances in perovskite-type oxides for energy conversion and storage applications. Adv Energy Mater 11 (2):2000459

[5] Bian J, Li Z, Li N, Sun C (2019) Oxygen deficient $LaMn_{0.75}Co_{0.25}O_{3-\delta}$ nanofibers as an efficient electrocatalyst for oxygen evolution reaction and zinc–air batteries. Inorg chem 58 (12):8208-8214

[6] Chen C, Kang Y, Huo Z et al (2014) Highly crystalline multimetallic nanoframes with three-dimensional electrocatalytic surfaces. Science 343 (6177):1339-1343

[7] Han G, Liu Y, Gao J et al (2018) Local plant-derived carbon sheets as sustainable catalysts for efficient oxygen reduction reaction. ACS Sustain Chem En 7 (2):2107-2115

[8] Bian J, Su R, Yao Y et al (2019) Mg doped perovskite $LaNiO_3$ nanofibers as an efficient bifunctional catalyst for rechargeable zinc–air batteries. ACS Appl Energy Mater 2 (1):923-931

[9] Jiao D, Ma Z, Li J et al (2020) Test factors affecting the performance of zinc–air battery. J Energy Chem 44:1-7

[10] Han J, Meng X, Lu L, Wang ZL, Sun C (2020) Triboelectric nanogenerators powered electrodepositing tri-functional electrocatalysts for water splitting and rechargeable zinc-air battery: A case of Pt nanoclusters on NiFe-LDH nanosheets. Nano Energy 72:104669

[11] Zhu Y, Sun W, Chen W et al (2018) Scale-Up Biomass Pathway to Cobalt Single-Site Catalysts Anchored on N-Doped Porous Carbon Nanobelt with Ultrahigh Surface Area. Adv Funct Mater 28 (37):1802167

[12] Han J, Bian J, Sun C (2020) Recent Advances in Single-Atom Electrocatalysts for Oxygen Reduction Reaction. Research: 9512763

[13] Wang R, Yang Y, Zhao Y et al (2021) Multiscale structural engineering of atomically dispersed FeN4 electrocatalyst for proton exchange membrane fuel cells. J Energy Chem 58:629-635

[14] Han J, Meng X, Lu L et al (2019) Single-Atom $Fe\text{-}N_x\text{-}C$ as an Efficient Electrocatalyst for Zinc–Air Batteries. Adv Funct Mater 29 (41):1808872

[15] Du L, Zhang G, Liu X et al (2020) Biomass-derived nonprecious metal catalysts for oxygen reduction reaction: The demand-oriented engineering of active sites and structures. Carbon Energy 2 (4):561-581

[16] Han H, Wang X, Zhang X (2021) A hierarchically ordered porous nitrogen-doped carbon catalyst with densely accessible $Co\text{-}N_x$ active sites for efficient oxygen reduction reaction. Micropor Mesopor Mater 317:111002

[17] Du C, Liu X, Ye G et al (2019) Balancing the micro-mesoporosity for activity maximization of N-doped carbonaceous electrocatalysts for the oxygen reduction reaction. ChemSusChem 12 (5):1017-1025

[18] Du C, Gao Y, Wang J, Chen W (2020) A new strategy for engineering a hierarchical porous carbon-anchored Fe single-atom electrocatalyst and the insights into its bifunctional catalysis for flexible rechargeable Zn–air batteries. J Mater Chem A 8

(19):9981-9990

[19] Wei Q, Zhang G, Yang X et al (2017) 3D porous Fe/N/C spherical nanostructures as high-performance electrocatalysts for oxygen reduction in both alkaline and acidic media. ACS appl mater inter 9 (42):36944-36954

[20] Jiang T, Luan W, Ren Y et al (2020) Synergistic heat treatment derived hollow-mesoporous-microporous Fe–N–C-SHT electrocatalyst for oxygen reduction reaction. Micropor Mesopor Mater 305:110382

[21] Mei H, Yang M, Shen Y et al (2019) Non-covalent pre-organization of molecular precursors: A facile approach for engineering structures and activities of pyrolyzed Co-NC electrocatalysts. Carbon 144:312-320

[22] Zheng X, Shen G, Wang C et al (2017) Bio-inspired Murray materials for mass transfer and activity. Nat commun 8 (1):1-9

[23] Liang K, Xu Y, Wang L, Liu Y, Liu YN (2019) Alkali-Driven Assembly of Protein-Rich Biomass Boosts the Electrocatalytic Activity of the Derived Carbon Materials for Oxygen Reduction. ChemCatChem 11 (19):4822-4829

[24] Qian W, Sun F, Xu Y et al (2014) Human hair-derived carbon flakes for electrochemical supercapacitors. Energy Environ Sci 7 (1):379-386

[25] Li Y, Liu D, Gan J et al (2019) Sustainable and Atomically Dispersed Iron Electrocatalysts Derived from Nitrogen-and Phosphorus-Modified Woody Biomass for Efficient Oxygen Reduction. Adv Mater Interfaces 6 (4):1801623

[26] Niu Y, Teng X, Gong S, Chen Z (2020) A bimetallic alloy anchored on biomass-derived porous N-doped carbon fibers as a self-supporting bifunctional oxygen electrocatalyst for flexible Zn–air batteries. J Mater Chem A 8 (27):13725-13734

[27] Fang W, Bai Z, Yu X, Zhang W, Wu M (2020) Pollen-derived porous carbon decorated with cobalt/iron sulfide hybrids as cathode catalysts for flexible all-solid-state rechargeable Zn–air batteries. Nanoscale 12 (21):11746-11758

[28] Zhang G, Liu X, Wang L et al (2019) B, N-Doped Defective Carbon Entangled Fe_3C Nanoparticles as the Superior Oxygen Reduction Electrocatalyst for Zn–Air Batteries. ACS Sustain Chem Eng 7 (23):19104-19112

[29] Peng X, Zhang L, Chen Z et al (2019) Hierarchically porous carbon plates derived from wood as bifunctional ORR/OER electrodes. Adv Mater 31 (16):1900341

[30] Ye Y-Y, Qian T-T, Jiang H (2020) Co-Loaded N-Doped Biochar as a High-Performance Oxygen Reduction Reaction Electrocatalyst by Combined Pyrolysis of Biomass. Ind Eng Chem Res 59 (35):15614-15623

[31] Jiang W-J, Gu L, Li L et al (2016) Understanding the high activity of Fe–N–C electrocatalysts in oxygen reduction: Fe/Fe_3C nanoparticles boost the activity of Fe–N x. J Am Chem Soc 138 (10):3570-3578

[32] Xiao C, Gaddam RR, Wu Y et al (2021) Improvement of the electrocatalytic performance of FeP in neutral electrolytes with Fe nanoparticles. Chem Eng J 408:127330

[33] Zhang C, Liu J, Ye Y et al (2018) Fe–N-doped mesoporous carbon with dual active sites loaded on reduced graphene oxides for efficient oxygen reduction catalysts. ACS appl mater inter 10 (3):2423-2429

[34] Zhang Z, Sun J, Wang F, Dai L (2018) Efficient oxygen reduction reaction (ORR)

catalysts based on single iron atoms dispersed on a hierarchically structured porous carbon framework. Angew Chem 130 (29):9176-9181

[35] Tang Z, Pei Z, Wang Z et al (2018) Highly anisotropic, multichannel wood carbon with optimized heteroatom doping for supercapacitor and oxygen reduction reaction. Carbon 130:532-543

[36] Kaare Kt, Yu E, Volperts A et al (2020) Highly Active Wood-Derived Nitrogen-Doped Carbon Catalyst for the Oxygen Reduction Reaction. ACS omega 5 (37):23578-23587

[37] Pi L, Jiang R, Cai W et al (2020) Bionic Preparation of CeO_2-Encapsulated Nitrogen Self-Doped Biochars for Highly Efficient Oxygen Reduction. ACS Appl Mater Inter 12 (3):3642-3653

[38] Zhang Z, Gao X, Dou M, Ji J, Wang F (2017) Biomass Derived N-Doped Porous Carbon Supported Single Fe Atoms as Superior Electrocatalysts for Oxygen Reduction. Small 13 (22):1604290

[39] Tian L, Ji D, Zhang S et al (2020) A Humidity-Induced Nontemplating Route toward Hierarchical Porous Carbon Fiber Hybrid for Efficient Bifunctional Oxygen Catalysis. Small 16 (23):2001743

[40] Shao C, Zhuang S, Zhang H et al (2020) Enhancement of Mass Transport for Oxygen Reduction Reaction Using Petal-Like Porous Fe-NC Nanosheet. Small:2006178

[41] Wang Z, Yu J, Xu P, Tan B, Wang J (2020) Embedding activated carbon nanospheres into polymer-derived porous carbon networks to boost electrocatalytic oxygen reduction. Chem Commun 56 (68):9791-9794

[42] Xu J, Lai S, Qi D et al (2020) Atomic Fe-Zn dual-metal sites for high-efficiency pH-universal oxygen reduction catalysis. Nano Res:1-8

[43] Wu Y, Chen Y, Wang H et al (2018) Efficient ORR electrocatalytic activity of peanut shell-based graphitic carbon microstructures. J Mater Chem A 6 (25):12018-12028

[44] Lv X, Chen Y, Wu Y et al (2019) A Br-regulated transition metal active-site anchoring and exposure strategy in biomass-derived carbon nanosheets for obtaining robust ORR/HER electrocatalysts at all pH values. J Mater Chem A 7 (47):27089-27098

[45] Dinh KN, Gomes VG (2019) Iodine doped composite with biomass carbon dots and reduced graphene oxide: a versatile bifunctional electrode for energy storage and oxygen reduction reaction. J Mater Chem A 7 (39):22650-22662

[46] Sudarsono W, Wong WY, Loh KS et al (2020) Sengon wood-derived RGO supported Fe-based electrocatalyst with stabilized graphitic N-bond for oxygen reduction reaction in acidic medium. Int J Hydrog Energy 45 (43):23237-23253

[47] Tan Z, Li H, Feng Q et al (2019) One-pot synthesis of Fe/N/S-doped porous carbon nanotubes for efficient oxygen reduction reaction. J Mater Chem A 7 (4):1607-1615

[48] Choi CH, Lim H-K, Chung MW et al (2014) Long-range electron transfer over graphene-based catalyst for high-performing oxygen reduction reactions: importance of size, N-doping, and metallic impurities. J Am Chem Soc 136 (25):9070-9077

[49] Huang Z, Pan H, Yang W et al (2018) In situ self-template synthesis of Fe–N-doped double-shelled hollow carbon microspheres for oxygen reduction reaction. ACS

nano 12 (1):208-216

[50] Unni SM, Illathvalappil R, Bhange SN, Puthenpediakkal H, Kurungot S (2015) Carbon nanohorn-derived graphene nanotubes as a platinum-free fuel cell cathode. ACS appl mater inter7 (43):24256-24264

[51] Mamtani K, Jain D, Dogu D et al (2018) Insights into oxygen reduction reaction (ORR) and oxygen evolution reaction (OER) active sites for nitrogen-doped carbon nanostructures (CN_x) in acidic media. Appl Catal B: Environ 220:88-97

[52] Xiao M, Zhu J, Ma L et al (2018) Microporous framework induced synthesis of single-atom dispersed Fe-NC acidic ORR catalyst and its in situ reduced Fe-N_4 active site identification revealed by X-ray absorption spectroscopy. Acs Catal 8 (4):2824-2832

[53] Lin L, Zhu Q, Xu A-W (2014) Noble-metal-free Fe–N/C catalyst for highly efficient oxygen reduction reaction under both alkaline and acidic conditions. J Am Chem Soc 136 (31):11027-11033

[54] Hu K, Tao L, Liu D et al (2016) N/C nanosheets as highly efficient electrocatalysts for oxygen reduction reaction, ACS Appl. Mater. Interfaces 8:19379-19385

[55] Yang Z, Chen B, Chen W et al (2019) Directly transforming copper (I) oxide bulk into isolated single-atom copper sites catalyst through gas-transport approach. Nat commun 10 (1):1-7

[56] Diao J, Qiu Y, Liu S et al (2020) Interfacial Engineering of W_2N/WC Heterostructures Derived from Solid-State Synthesis: A Highly Efficient Trifunctional Electrocatalyst for ORR, OER, and HER. Adv Mater 32 (7):1905679

[57] Cui L, Cui L, Li Z et al (2019) A copper single-atom catalyst towards efficient and durable oxygen reduction for fuel cells. J Mater Chem A 7 (28):16690-16695

[58] Tian L, Ji D, Zhang S et al (2020) A Humidity-Induced Nontemplating Route toward Hierarchical Porous Carbon Fiber Hybrid for Efficient Bifunctional Oxygen Catalysis. Small:2001743

[59] Chen P, Zhou T, Xing L et al (2017) Atomically dispersed iron–nitrogen species as electrocatalysts for bifunctional oxygen evolution and reduction reactions. Angew Chem 129 (2):625-629

[60] Wang M, Qian T, Zhou J, Yan C (2017) An efficient bifunctional electrocatalyst for a zinc–air battery derived from Fe/N/C and bimetallic metal–organic framework composites. ACS Appl Mater Inter 9 (6):5213-5221

[61] Wang Z, Jin H, Meng T et al (2018) Fe, Cu-Coordinated ZIF-Derived Carbon Framework for Efficient Oxygen Reduction Reaction and Zinc–Air Batteries. Adv Funct Mater 28 (39):1802596

[62] Lei Y, Yang F, Xie H, Lei Y et al (2020) Biomass in situ conversion to Fe single atomic sites coupled with Fe_2O_3 clusters embedded in porous carbons for the oxygen reduction reaction. J Mater Chem A 8 (39):20629-20636

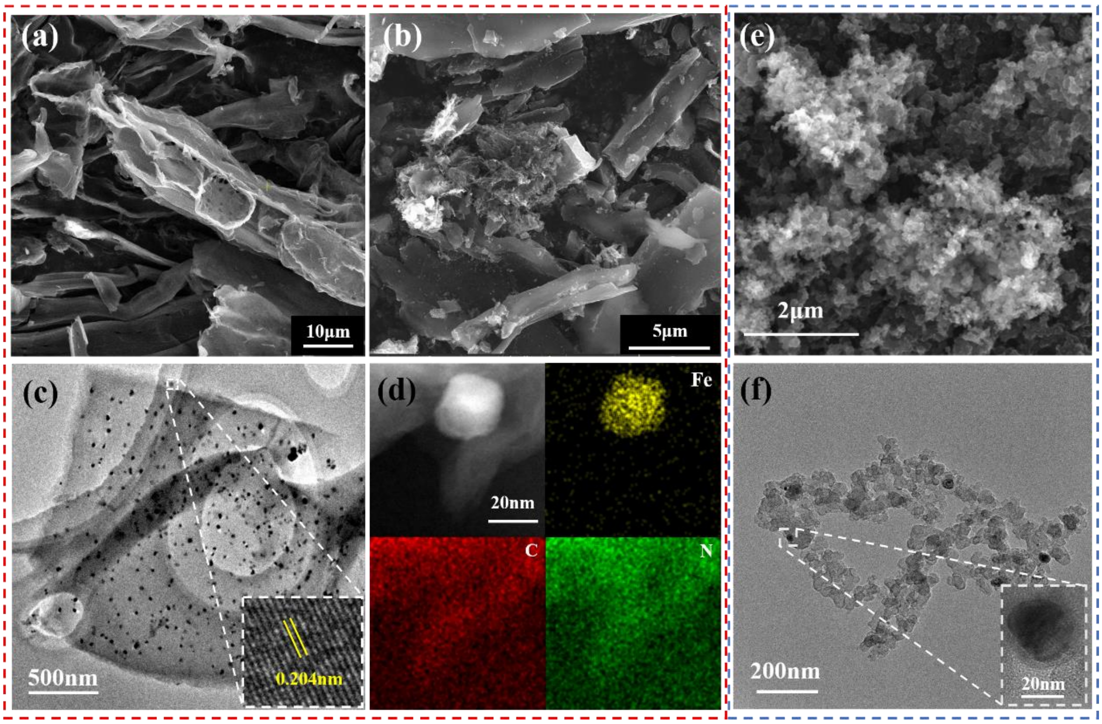

Figure 1. Characterization of Fe-N-C_{wood}. SEM images of N-C_{wood} (a) and Fe-N-C_{wood} (b); TEM images of Fe-N-C_{wood}, the inset shows the crystalline lattice of the marked particle (c); HAADF-TEM image of particles in Fe-N-C_{wood} coupled with electron energy loss spectroscopy (d). SEM images (e) and TEM images (f) of Fe-N-$C_{XC-72.}$

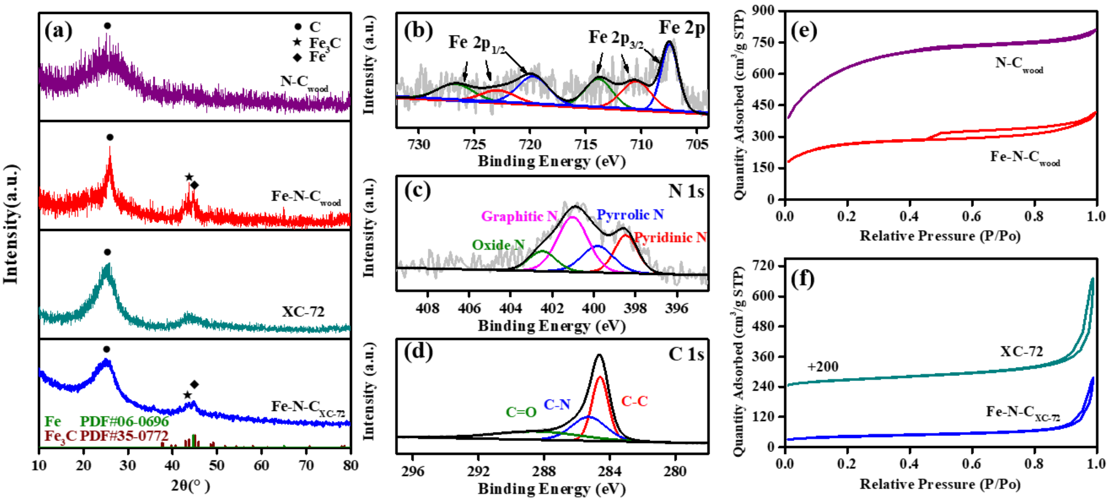

Figure 2. Chemical state and textural property of Fe-N-C$_{wood}$. XRD patterns of N-C$_{wood}$, Fe-N-C$_{wood}$, XC-72 and Fe-N-C$_{XC-72}$ (a); high-resolution Fe 2p, N 1s and C 1s XPS spectra of Fe-N-C$_{wood}$ (b-d); N_2 sorption isotherm of N-C$_{wood}$, Fe-N-C$_{wood}$, XC-72 and Fe-N-C$_{XC-72}$ (e,f).

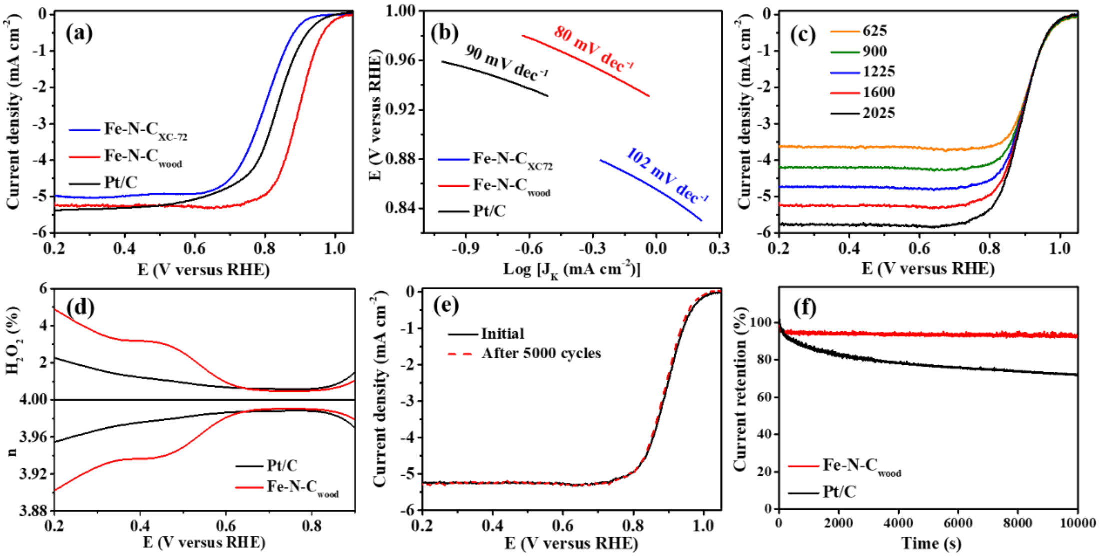

Figure 3. Electrochemical evaluation of Fe-N-C$_{wood}$ in 0.1 M KOH. Polarization curves of Fe-N-C$_{XC-72}$, Fe-N-C$_{wood}$ and Pt/C (a); Corresponding Tafel plots (b); LSV curves of Fe-N-C$_{wood}$ at different rotating rates (c); Electron transfer number (n, bottom) and H_2O_2 yield (top) versus potential (d); LSV curves of Fe-N-C$_{wood}$ in O_2-saturated 0.1 M KOH before and after 5,000 cycles (e); Chronoamperometric response of Fe-N-C$_{wood}$ and Pt/C (f).

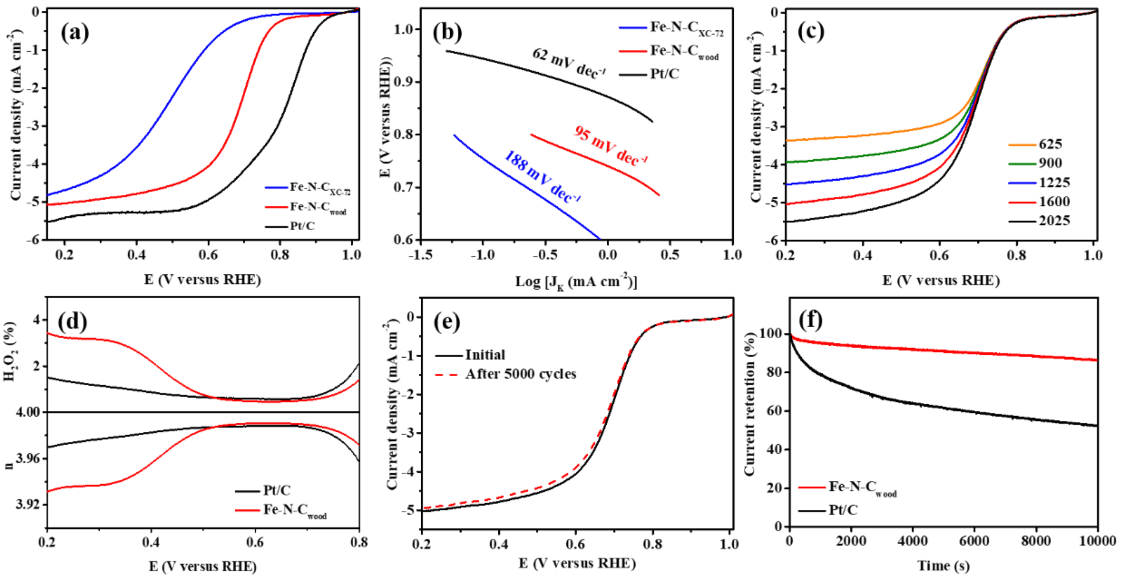

Figure 4. Electrochemical evaluation of Fe-N-C$_{wood}$ in 0.1 M $HClO_4$. Polarization curves of Fe-N-C$_{XC-72}$, Fe-N-C$_{wood}$ and Pt/C (a); Corresponding Tafel plots (b); LSV curves of Fe-N-C$_{wood}$ at different rotating rates (c); Electron transfer number (n, bottom) and H_2O_2 yield (top) versus potential (d); LSV curves of Fe-N-C$_{wood}$ in O_2-saturated 0.1 M $HClO_4$ before and after 5,000 cycles (e); Chronoamperometric response of Fe-N-C$_{wood}$ and Pt/C (f).

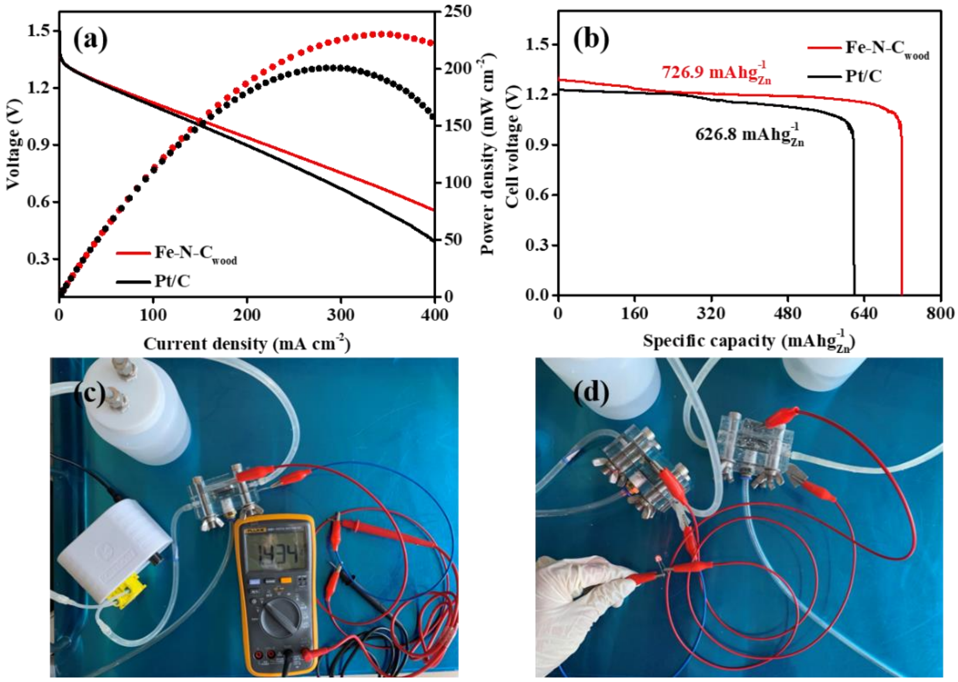

Figure 5. Zn-air battery performance of Fe-N-C$_{wood}$. Discharge polarization and corresponding power density plots of Fe-N-C$_{wood}$ and Pt/C based Zn-air battery (a). Specific capacities of Fe-N-C$_{wood}$ and Pt/C-based Zn-air battery (b). Fe-N-C$_{wood}$ based liquid Zn–air battery (c). LED powered by two liquid Zn–air batteries with the Fe-N-C$_{wood}$ heterostructures electrocatalyst (d).

Table 1. Comparison of the ORR activity between Fe-N-C_{wood} and other biomass-based catalysts under alkaline condition (0.1 M KOH) in literature.

Sample	Electrolyte	E_{onset} (V)	$E_{1/2}$ (V)	Reference
Fe-N-C_{wood}	0.1 M KOH	0.98	0.90	**This work**
TARC-N	0.1 M KOH	0.98	0.86	[35]
N/E-HPC-900	0.1 M KOH	0.99	0.85	[29]
Co@NCBC	0.1 M KOH	0.98	0.86	[30]
AWC-1	0.1 M KOH	0.92	0.85	[36]
NiFe@N-CFs	0.1 M KOH	0.94	0.82	[26]
Fe−N−C/rGO)	0.1 M KOH	0.94	0.81	[33]
BC-Ce-2	0.1 M KOH	0.90	0.84	[37]
Co–Fe–S@NSRPC	0.1 M KOH	-	0.80	[27]
SA-Fe/NHPC	0.1 M KOH	-	0.87	[38]
Co/Co_3O_4@HPCNF-50	0.1 M KOH	0.92	0.82	[39]
FeNC-D0.5	0.1 M KOH	-	0.87	[40]
AC/TBC(O)	0.1 M KOH	0.85	0.74	[41]
Fe-Zn-SA/NC	0.1 M KOH	-	0.85	[42]
CoOP@bio-C	0.1 M KOH	0.91	0.81	[43]
CoTBrPP@bio-C	0.1 M KOH	0.93	0.85	[44]
HI-RGO/CDs	0.1 M KOH	0.93	0.77	[45]

Table 2. Comparison of the ORR activity between Fe-N-C_{wood} and other noble metal free catalysts under alkaline condition (0.1 M $HClO_4$) in literature.

Sample	Electrolyte	E_{onset} (V)	$E_{1/2}$ (V)	Reference
Fe-N-C_{wood}	0.1 M $HClO_4$	0.81	0.70	**This work**
Fe-Pani-RGO 2 py	0.1 M $HClO_4$	0.82	0.74	[46]
Fe/N/S-PCNTs	0.5 M H_2SO_4	0.80	0.62	[47]
bNGr	0.1 M $HClO_4$	0.88	0.70	[48]
Fe-N-DSC	0.5 M H_2SO_4	0.81	0.65	[49]
Fe-N-CNT	0.1 M $HClO_4$	0.77	0.46	[50]
CNx	0.1 M $HClO_4$	0.80	0.67	[51]
Fe-N-C-950	0.1 M $HClO_4$	0.92	0.78	[52]
Fe-N-C	0.1 M $HClO_4$	0.80	0.60	[53]
S-Fe/N/C	0.1 M $HClO_4$	0.83	0.66	[54]

Table 3. Comparison of the peak power density of Fe-N-C$_{wood}$ based Zn-air battery and other reported Zn-air batteries in literature.

Sample	Loading (mg cm^{-2})	Peak power density (mW cm^{-2})	Reference
Fe-N-C$_{wood}$	1	231	**This work**
Cu ISAS/NC	1	280	[55]
Cu SAs/NC-900	1	242	[3]
W_2N/WC	0.6	172	[56]
Fe-Zn-SA/NC	2	167.2	[42]
Cu SAC	2	196	[57]
Co/Co_3O_4@HPCNF-50	1	102.5	[58]
S,N-Fe/N/C-CNT	1.25	102.7	[59]
CoTBrPP@bio-C	1	100	[44]
Fe/N/C@BMZIF	1	235	[60]
Cu@Fe-N-C	1	92	[61]
Fe$_{SA}$/FeO$_{NC}$/NSC	1	179.0	[62]